4. Messenger, S. & Bernatowicz, T. J. Search for presolar silicates in Acfer 094. *Meteorit. Planet. Sci.* **35**, A109 (2000).

5. Alexander, C. M. O'D., Nittler, L. R. & Tera, F. The search of presolar silicates and the ^{54}Cr carrier. *Lunar Planet. Sci.* [CD-ROM] **XXXII**, 2191 (2001).

6. Mostefaoui, S., Hoppe, P., Marhas, K. K. & Gröner, E. Search for *in situ* presolar oxygen-rich dust in meteorites. *Meteorit. Planet. Sci.* **38**, A99 (2003).

7. Nittler, L. R., Alexander, C. M. O'D., Gao, X., Walker, R. M. & Zinner, E. Stellar sapphires: The properties and origins of presolar Al_2O_3 in meteorites. *Astrophys. J.* **483**, 475–495 (1997).

8. Lugaro, M., Zinner, E., Gallino, R. & Amari, S. Si isotopic ratios in mainstream presolar SiC grains revisited. *Astrophys. J.* **527**, 369–394 (1999).

9. Messenger, S., Keller, L. P., Stadermann, F. J., Walker, R. M. & Zinner, E. Samples of stars beyond the solar system: silicate grains in interplanetary dust. *Science* **300**, 105–108 (2003).

10. Newton, J. *et al.* Acfer 094, a uniquely primitive carbonaceous chondrite from the Sahara. *Meteoritics* **30**, 47–56 (1995).

11. Greshake, A. The primitive matrix components of the unique carbonaceous chondrite Acfer 094; a TEM study. *Geochim. Cosmochim. Acta* **61**, 437–452 (1997).

12. Krot, A. N., Meibom, A., Weisberg, M. K. & Keil, K. The CR chondrite clan: implications for early solar system processes. *Meteorit. Planet. Sci.* **37**, 1451–1490 (2002).

13. Yurimoto, H., Nagashima, K. & Kunihiro, T. High precision isotope micro-imaging of materials. *Appl. Surf. Sci.* **203–204**, 793–797 (2003).

14. Kunihiro, T., Nagashima, K. & Yurimoto, H. Microscopic oxygen isotopic homogeneity/heterogeneity in the matrix from the Vigarano CV3 chondrite. *Geochim. Cosmochim. Acta* (submitted).

15. Hoppe, P. & Ott, U. in *Astrophysical Implications of the Laboratory Study of Presolar Materials* (eds Bernatowicz, T. J. & Zinner, E.) 27–58 (AIP Press, New York, 1997).

16. Huss, G. R., Meshik, A. P., Smith, J. B. & Hohenberg, C. M. Presolar diamond, silicon carbide, and graphite in carbonaceous chondrites: Implications for thermal processing in the solar nebula. *Geochim. Cosmochim. Acta* **67**, 4823–4848 (2003).

17. Dai, Z. R. *et al.* Possible *in situ* formation of meteoritic nanodiamonds in the early Solar System. *Nature* **418**, 157–159 (2002).

18. Jessberger, E. K. *et al.* in *Interplanetary Dust* (eds Grün, E., Gustafson, B. Å. S., Dermott, S. F. & Fechtig, H.) 253–294 (Springer, Berlin, 2001).

19. Bradley, J. P. & Brownlee, D. E. Cometary particles: thin sectioning and electron beam analysis. *Science* **231**, 1542–1544 (1986).

20. Hewins, R. H. in *Chondrules and the Protoplanetary Disk* (eds Hewins, R. H., Jones, R. H. & Scott, E. R. D.) 3–9 (Cambridge Univ. Press, Cambridge, 1996).

21. Itoh, S. & Yurimoto, H. Contemporaneous formation of chondrules and refractory inclusions in the early Solar System. *Nature* **423**, 728–731 (2003).

22. Bischoff, A. *et al.* New carbonaceous and type 3 ordinary chondrites from the Sahara Desert. *Meteoritics* **26**, 318 (1991).

23. Clayton, R. N. & Mayeda, T. K. Oxygen isotope studies of carbonaceous chondrites. *Geochim. Cosmochim. Acta* **63**, 2089–2104 (1999).

....

Carbon nanotubes as nanoscale mass conveyors

B. C. Regan[1,3], **S. Aloni**[1,3], **R. O. Ritchie**[3,2], **U. Dahmen**[3,4] **& A. Zettl**[1,3]

[1]Department of Physics, [2]Department of Materials Science and Engineering, University of California at Berkeley, California 94720, USA
[3]Materials Sciences Division, [4]National Center for Electron Microscopy, Lawrence Berkeley National Laboratory, Berkeley, California 94720, USA

....

The development of manipulation tools that are not too 'fat' or too 'sticky' for atomic scale assembly is an important challenge facing nanotechnology[1]. Impressive nanofabrication capabilities have been demonstrated with scanning probe manipulation of atoms[2–5] and molecules[4,6] on clean surfaces. However, as fabrication tools, both scanning tunnelling and atomic force microscopes suffer from a loading deficiency: although they can manipulate atoms already present, they cannot efficiently deliver atoms to the work area. Carbon nanotubes, with their hollow cores and large aspect ratios, have been suggested[7,8] as possible conduits for nanoscale amounts of material. Already much effort has been devoted to the filling of nanotubes[8–11] and the application of such techniques[12,13]. Furthermore, carbon nanotubes have been used as probes in scanning probe microscopy[14–16]. If the atomic placement and manipulation capability already demonstrated by scanning probe microscopy could be combined with a nanotube delivery system, a formidable nanoassembly tool would result. Here we report the achievement of controllable, reversible atomic scale mass transport along carbon nanotubes, using indium metal as the prototype transport species. This transport process has similarities to conventional electromigration, a phenomenon of critical importance to the semiconductor industry[17,18].

Our experiments are performed inside a JEOL-2010 transmission electron microscope (TEM) equipped with a piezo-driven nanomanipulation stage (Nanofactory Instruments AB). Indium metal is thermally evaporated *ex situ* onto a boule of arc-grown multiwalled carbon nanotubes (MWNTs), which decorates the nanotubes with isolated indium nanocrystals[19]. The coated boule is then fixed to the sample side of the TEM stage. Inside the TEM, under high vacuum conditions, an individual nanotube or bundle is approached with a freshly etched tungsten tip mounted on the nanomanipulator, and physical contact is made between the tip and the free end of the nanotube. Applying a voltage between the tip and the sample holder establishes an electrical circuit through the subject tube, and injects thermal energy into the system via Joule heating. By increasing the applied voltage, the local temperature can be easily increased past the melting point of the indium particles decorating the tube. Further manipulation of the voltage produces dramatic mass transport between these nanoparticles, which serve as mass reservoirs. The transport process is recorded using real-time TEM video imaging.

Figure 1 gives a series of video frames illustrating the transport process. A single MWNT, clean except for resident indium particles, spans each image from left to right. During the three-minute period shown, a current of ~40 μA is passing through the MWNT. The first frame of Fig. 1 shows three large indium particles, separated by about 100 nm, and several smaller ones. The dark contrast and nearly round shapes indicate that the particles are molten. As the experiment proceeds, particles to the left are generally getting smaller, while those to the right grow. Tracking the central large particle in particular, we see that it grows between the first and second frames—while there are still particles to its left—but shrinks thereafter. Qualitative inspection suggests a near unity correlation
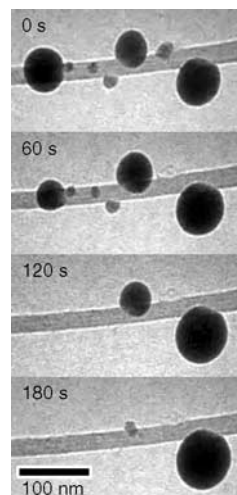

Figure 1 Four TEM video images, spaced by one-minute increments, showing left-to-right indium transport on a single MWNT. The tip (anode) is out of view to the left and the sample electrode (cathode) is out of view to the right. The measured circuit resistance is ~49 kΩ, most of which is presumably concentrated at the tip–MWNT contact.

between mass losses on the left and mass gains to the right.

The same transport process demonstrated in Fig. 1 can occur over a much larger length scale, as shown in Fig. 2. Here the tungsten tip is visible at the extreme left of the images, and the sample boule with protruding, indium-decorated MWNTs is on the far right. Spanning the tip–boule gap is a MWNT bundle 3.3 μm long. Figur 2a shows a round indium particle (arrowed) on the subject bundle near the tip. Applying 1.8 V between the tip and sample holder drives ~50 μA through the bundle, with the result shown in Fig. 2b: the particle near the tip has disappeared, and over 2 μm away, two new indium particles have appeared.

It is tempting to infer that a temperature gradient drives the mass transport along the nanotubes. In Fig. 1, and Fig. 2a and b, the presumed high-resistance point, or 'hot spot', is on the left side of the images. Thus in these figures mass is consistently moving towards cooler locales. To test this hypothesis, we reversed the direction of the supplied current, which, by virtue of Joule heating I^2R, maintains the same temperature gradient. Figure 2c shows the result: the two new particles vanish, and the original particle near the tip reappears, growing to its original size. Thus the voltage gradient, rather than the thermal gradient, determines the direction of mass transport.

Figures 1 and 2 are highly suggestive of mass conservation. Applying an automated image processing routine to the video data from such experiments, we extract particle areas and, approximating the particles as spheres, thereby determine their masses quantitatively (mass = $(7\,\mathrm{g\,cm}^{-3})\,(4\pi/3)\,(\mathrm{area}/\pi)^{3/2}$). We find that total indium mass is conserved to a high degree of accuracy (±5%) during the transport process. Indeed, apparent lack of mass conservation invariably originates from failure to use a wide enough field of view, that is, to include all the participating particles.

Because both the rate and direction of mass transport depend on the external electrical drive, precise control of a mass distribution is possible. Figure 3 illustrates how two indium particles on a MWNT bundle alternately grow and shrink as they exchange mass in response to a square-wave forcing function. The direction of indium transport is again towards the cathode. Although square-wave control is shown here for simplicity's sake, the mass transfer rate can be regulated to any desired level by adjusting the voltage. Because of the high thermal conductivity of the nanotube, driving the voltage to zero rapidly quenches the mass transport. Mass can be delivered, in principle atom-by-atom, until a final, pre-selected particle size is achieved. This has obvious consequences for tailoring nanoscale mass distributions for (for example) optical, electronic or mechanical applications. By delivering material to its end, it is possible to use the nanotube as a 'nano soldering iron'. Besides

indium, we have also performed mass transport experiments with Au, Pt, Sn and Sn-In alloy.

We have developed a quantitative model that accounts for the observed dynamics of the transport process. In our model, indium atoms move between particles as the constituents of a two-dimensional gas on the surface of the nanotube. At a given temperature, an indium particle maintains an equilibrium indium surface concentration on the host nanotube at its attachment point. On the nanotube the metal atoms move in a thermally activated diffusion process, but with an important directional bias supplied by the applied electric field. Thus the electric field can shift the surface concentration of indium above or below the thermodynamic equilibrium point at a given site, and thereby dictate whether a particle at that site will grow or shrink. Likewise, nearby particles, which act as mass sources and sinks, influence the fate of a particle at a given location.

Figure 4a shows an analogy for the model. Mass reservoirs, representing indium particles at local temperature T_i, are connected by mass conveyors. Each conveyor moves mass at a fixed rate J_{ij} that is a function of electric field and temperature. Conveyors nearer the hot spot move mass more rapidly. If mass is moving down a temperature gradient, an intermediate reservoir will fill as its source conveyor provides mass faster than its drain conveyor takes it away. Once the upstream reservoir is exhausted, the intermediate reservoir will begin to empty at the rate set by its drain conveyor. As an atom might diffuse past a particle without joining it, at each reservoir we also allow for a 'bypass' probability (bypasses are not depicted in Fig. 4a).

Figure 4b schematically depicts an experiment, similar to those presented above, that demonstrates the utility of the mass conveyor model. A tip extension touches a small nanotube bundle that subsequently supports indium particles at four different positions, I–IV. Initially the indium is concentrated in particle I. The tip voltage is ramped to 1.7 V relative to the sample boule and mass begins moving from left to right, as particles closer to the sample electrode grow at the expense of those near the tip. After the voltage ramp, the applied power is consistently ~45 μW. TEM video of the mass transport process is available as Supplementary movie S1.

Using the mass-determination routine, a mass versus time plot has been generated for particles I–IV from Supplementary movie S1. The relevant data are shown as discrete symbols in Fig. 4c. Gaps in the data occur because the video was taken at high magnification, where the field of view is large enough to contain only one or two
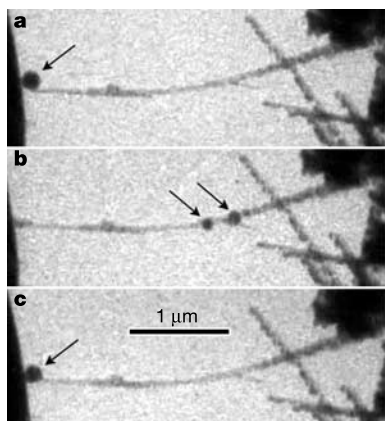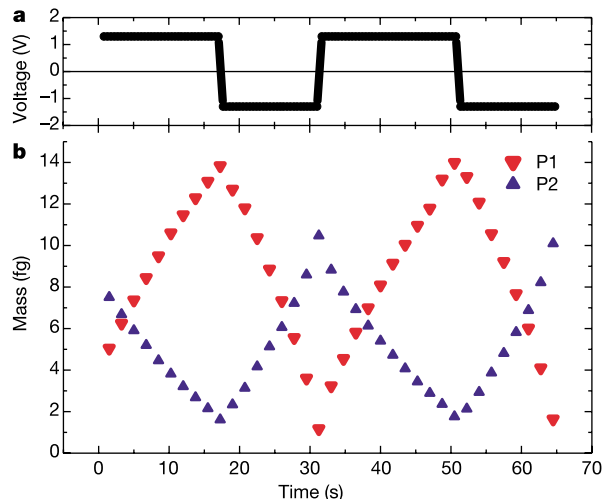
Figure 2 Time series of three TEM video images showing reversible indium transport over a distance of more than 2 μm. By applying appropriate current to the carbon nanotube pictured, indium is moved from left (**a**) to right (**b**) and back again (**c**). Arrows identify the relevant particles.

Figure 3 Controllable, reversible indium transport. **a**, Control voltage (±1.3 V) as a function of time. **b**, Particle masses as a function of time. On the MWNT bundle, particle 1 (P1) is located nearer the tip than particle 2 (P2).

particle positions simultaneously. Despite its fragmentary nature, the data set is quite revealing. For example, the curves are constructed of remarkably linear segments. The constancy of these mass change rates suggests that surface energies, which vary with particle radius[20], are not playing a significant role in driving the transport process, down to at least the femtogram level (1 fg indium $\sim 5 \times 10^6$ atoms $\sim$ 30-nm-radius sphere). Similarly, indium concentrations only affect transfer rates in a binary sense: the presence or absence of a particle, but not its size, influences the growth of its neighbours. Thus the disappearance of particle II near time $t = 14$ s changes the growth rate of particle III from a positive value to a negative one, but its slow diminution has no effect.

To compare the predictions of the mass conveyor model to the experimental data of Fig. 4c, seven non-zero input parameters are required. Four of these parameters are determined by linear fits on appropriate sections of the data: the initial mass of particle I, and the mass loss rates of particles I, II and III. The remaining three inputs (bypass probabilities for particles II, III and IV) are set by least squares minimization. Other aspects of the curves, for example, growth rates, axis intercepts and turnover points, then follow directly from mass conservation. The solid lines in Fig. 4c are the predictions of the mass conveyor model with these inputs. The
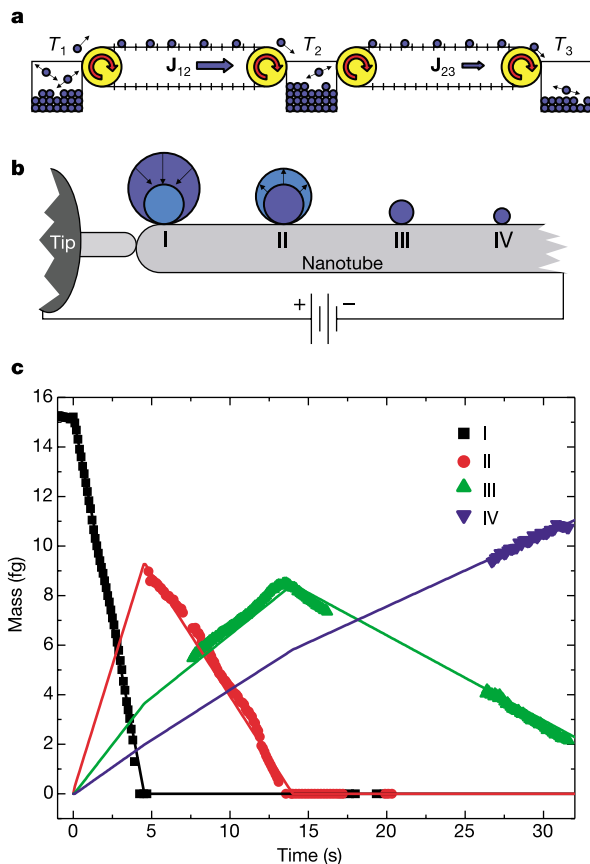
agreement between the model curves and the data is excellent. Kinks are predicted in the particle growth rates whenever another particle is exhausted, as seen in the mass curve of particle III at $t = 5$ s and dramatically at $t = 14$ s. Furthermore, the fits reveal that the probability for bypassing a particle in this system is small, as the best values are 11%, 14% and 15% for particles II, III and IV, respectively.

The conveyor analogy also anticipates the behaviour of this multi-reservoir system upon reversal of the applied voltage. When the voltage is reversed, the conveyors move mass in the opposite direction. However, because the temperature gradients do not change, conveyors nearer the tip continue to have higher throughput. Thus no intermediate particles will grow, as they are drained faster than they fill. Similarly, particles nearer the tip disappear faster than their more remote neighbours. When the voltage is reversed (see Supplementary movie S1), exactly these behaviours are observed. Particle III disappears before particle IV, and the mass re-condenses near the initial position of particle I.

The existence of preferred locations for particle growth, observed under a variety of substrate conditions, raises interesting issues. Particle growth is most reproducible at locations with seed indium, but regeneration also occurs where all the indium has been driven off. Such nucleation sites may be anchored by either refractory debris, such as indium oxide, or point defects intrinsic to the nanotube. Defects are relatively uncommon in these arc-grown carbon MWNTs, and thus are unlikely to be creating a contiguous preferred path on the nanotube surface. Interlayer transport of the indium through the carbon nanotubes can be ruled out, given that the intercalation of high quality carbon MWNTs requires serious degradation of their structural integrity[21]. (The resistance of nanotubes to hoop stress makes them much more difficult to intercalate than graphite.) It would be of interest to determine the indium concentration along the nanotubes during the transport process by using, for example, a TEM with analytical capability. Unfortunately our nanomanipulation stage is not configured for an analytical TEM, and we thus pose this as a challenge for future work.

Despite the successes of the model, questions remain about the exact nature of the driving mechanism. The data presented here establish that surface energies, which cause Ostwald ripening[22], and thermal gradients, which drive thermomigration[23], are of subordinate importance. Various authors have considered coupling between external species and electrical currents in carbon nanotubes[24–26]. Identifying the electric field as the most promising candidate driver allows useful comparisons with the known physics of electromigration. Within the electromigration model, electron transfer from the indium atoms to the substrate nanotubes accounts for the observed transport direction. Thus the 'direct' force from the electric field prevails over the 'wind' force created by momentum exchange with the charge carriers. Whereas indium electromigrates towards the anode in bulk, it moves towards the cathode on silicon surfaces[27,28], which are perhaps more analogous to this system. □

Figure 4 Reservoir-to-reservoir transport at constant applied power. **a**, Conveyor analogy for the transport process. The three mass reservoirs are in a temperature gradient, with $T_1 > T_2 > T_3$. The conveyors carry mass with throughput J, expressed in units of mass per time. Because J_{12} is larger than J_{23}, when the transport direction is as shown the second reservoir will accumulate mass until the first is emptied. When the transport direction is reversed, the second reservoir will lose mass regardless of the condition of its neighbours. **b**, Schematic depiction of the experimental set-up. Four indium particles distributed on a nanotube substrate grow and shrink as current is passed from the tungsten tip through the substrate. **c**, Particle masses as a function of time. Experimentally determined masses of the four particles are indicated with the symbols shown in the key. The solid curves are produced by a model that assumes constant mass transfer rates and mass conservation (see text).

1. Service, R. F. Is nanotechnology dangerous? *Science* **290**, 1526–1527 (2000).
2. Eigler, D. M. & Schweizer, E. K. Positioning single atoms with a scanning tunnelling microscope. *Nature* **344**, 524–526 (1990).
3. Crommie, M. F., Lutz, C. P. & Eigler, D. M. Confinement of electrons to quantum corrals on a metal surface. *Science* **262**, 218–220 (1993).
4. Bartels, L., Meyer, G. & Rieder, K. H. Basic steps of lateral manipulation of single atoms and diatomic clusters with a scanning tunneling microscope tip. *Phys. Rev. Lett.* **79**, 697–700 (1997).
5. Oyabu, N., Custance, O., Yi, I. S., Sugawara, Y. & Morita, S. Mechanical vertical manipulation of selected single atoms by soft nanoindentation using near contact atomic force microscopy. *Phys. Rev. Lett.* **90**, 176102 (2003).
6. Heinrich, A. J., Lutz, C. P., Gupta, J. A. & Eigler, D. M. Molecule cascades. *Science* **298**, 1381–1387 (2002).
7. Kral, P. & Tomanek, D. Laser-driven atomic pump. *Phys. Rev. Lett.* **82**, 5373–5376 (1999).
8. Supple, S. & Quirke, N. Rapid imbibition of fluids in carbon nanotubes. *Phys. Rev. Lett.* **90**, 214501 (2003).
9. Ajayan, P. M. & Iijima, S. Capillarity-induced filling of carbon nanotubes. *Nature* **361**, 333–334 (1993).
10. Dujardin, E., Ebbesen, T. W., Hiura, H. & Tanigaki, K. Capillarity and wetting of carbon nanotubes. *Science* **265**, 1850–1852 (1994).
11. Pederson, M. R. & Broughton, J. Q. Nanocapillarity in fullerene tubules. *Phys. Rev. Lett.* **69**, 2689–2692 (1992).

12. Gao, Y. H. & Bando, Y. Carbon nanothermometer containing gallium. *Nature* **415**, 599 (2002).
13. Ugarte, D., Chatelain, A. & deHeer, W. A. Nanocapillarity and chemistry in carbon nanotubes. *Science* **274**, 1897–1899 (1996).
14. Wong, S. S., Joselevich, E., Woolley, A. T., Cheung, C. L. & Lieber, C. M. Covalently functionalized nanotubes as nanometre-sized probes in chemistry and biology. *Nature* **394**, 52–55 (1998).
15. Wong, S. S., Harper, J. D., Lansbury, P. T. & Lieber, C. M. Carbon nanotube tips: High-resolution probes for imaging biological systems. *J. Am. Chem. Soc.* **120**, 603–604 (1998).
16. Dai, H. J., Hafner, J. H., Rinzler, A. G., Colbert, D. T. & Smalley, R. E. Nanotubes as nanoprobes in scanning probe microscopy. *Nature* **384**, 147–150 (1996).
17. Pierce, D. G. & Brusius, P. G. Electromigration: a review. *Microelectron. Reliab.* **37**, 1053–1072 (1997).
18. Collins, P. G., Hersam, M., Arnold, M., Martel, R. & Avouris, P. Current saturation and electrical breakdown in multiwalled carbon nanotubes. *Phys. Rev. Lett.* **86**, 3128–3131 (2001).
19. Cumings, J. P. *Electrical and Mechanical Properties of Carbon and Boron Nitride Nanotubes*. Ph.D. thesis, Univ. California, Berkeley (2002).
20. Adamson, A. W. & Gast, A. P. *Physical Chemistry of Surfaces* (Wiley, New York, 1997).
21. Duclaux, L. Review of the doping of carbon nanotubes (multiwalled and single-walled). *Carbon* **40**, 1751–1764 (2002).
22. Zinke-Allmang, M. Phase separation on solid surfaces: nucleation, coarsening and coalescence kinetics. *Thin Solid Films* **346**, 1–68 (1999).
23. Hummel, R. E. Electromigration and related failure mechanisms in integrated-circuit interconnects. *Int. Mater. Rev.* **39**, 97–111 (1994).
24. Kral, P. & Shapiro, M. Nanotube electron drag in flowing liquids. *Phys. Rev. Lett.* **86**, 131–134 (2001).
25. Ghosh, S., Sood, A. K. & Kumar, N. Carbon nanotube flow sensors. *Science* **299**, 1042–1044 (2003).
26. Mingo, N., Yang, L. & Han, J. Current-induced forces upon atoms adsorbed on conducting carbon nanotubes. *J. Phys. Chem. B* **105**, 11142–11147 (2001).
27. Yasunaga, H. & Natori, A. Electromigration on semiconductor surfaces. *Surf. Sci. Rep.* **15**, 205–280 (1992).
28. Kono, S., Goto, T., Ogura, Y. & Abukawa, T. Surface electromigration of metals on Si(001): In/Si(001). *Surf. Sci.* **420**, 200–212 (1999).

· ·

Interdecadal variation in the extent of South Pacific tropical waters during the Younger Dryas event

Thierry Corrège[1], Michael K. Gagan[2], J. Warren Beck[3], George S. Burr[3], Guy Cabioch[1] & Florence Le Cornec[4]

[1]*UR 055 Paléotropique, Institut de recherche pour le Développement (IRD), BPA5, Nouméa, New Caledonia*
[2]*Research School of Earth Sciences, The Australian National University, Canberra, ACT 0200, Australia*
[3]*NSF Arizona AMS Facility, Department of Physics, PAS Bldg #81, University of Arizona, Tucson, Arizona 85721, USA*
[4]*UR 055 Paléotropique, Institut de recherche pour le Développement (IRD), 32 avenue Henri Varagnat, 93143 Bondy Cedex, France*

....

During the Younger Dryas event, about 12,000 years ago, the Northern Hemisphere cooled by between 2 and 10 °C (refs 1, 2) whereas East Antarctica experienced warming[3]. But the spatial signature of the event in the southern mid-latitudes and tropics is less well known, as records are sparse and inconclusive[4–16]. Here we present high-resolution analyses of skeletal Sr/Ca and $^{18}O/^{16}O$ ratios for a giant fossil *Diploastrea heliopora* coral that was preserved in growth position on the raised reef terraces of Espiritu Santo Island, Vanuatu, in the southwestern tropical Pacific Ocean[17]. Our data indicate that sea surface temperatures in Vanuatu were on average 4.5 ± 1.3 °C cooler during the Younger Dryas event than today, with a significant interdecadal modu-

lation. The amplified annual cycle of sea surface temperatures, relative to today, indicates that cooling was caused by the compression of tropical waters towards the Equator. The positive correlation in our record between the oxygen isotope ratios of sea water and sea surface temperatures suggests that the South Pacific convergence zone, which brings ^{18}O-depleted precipitation to the area today, was not active during the Younger Dryas period.

Thirteen uranium-series age determinations distributed along the 2-m core drilled through the *Diploastrea* show that the specimen spans the age range 12,449 ± 18 (2σ) to 11,719 ± 58 (2σ) calendar years before present (BP), and that it lived during the Younger Dryas (YD) interval established from polar ice cores. Subsequently, more than 350 accelerator mass spectrometer radiocarbon (^{14}C) determinations were obtained on annual skeletal growth increments for calibration of the ^{14}C timescale[18]. The calculated $^{14}C/^{12}C$ ratios showed large decadal variations, which prompted us to conduct a multi-proxy geochemical study of the *Diploastrea* to investigate potential links with YD climate variability. Most coral palaeoclimate reconstructions are derived from geochemical tracers in skeletons of the coral genus *Porites*. However, *Diploastrea* is represented by a single species, *Diploastrea heliopora*, thus eliminating the possibility of inter-species differences in the behaviour of tested coral palaeothermometers, such as Sr/Ca and $^{18}O/^{16}O$ (δ^{18}O). Also, *Diploastrea* grows slowly (2–5 mm yr^{-1}) and typical 1–2-m-high colonies can live for hundreds of years, providing long records for palaeoclimatic studies.

To constrain the relationship between skeletal Sr/Ca and sea surface temperature (SST) for *Diploastrea*, we analysed two modern specimens: one from Alor, Indonesia, in the Western Pacific warm pool, and one from New Caledonia, in the southwestern tropical Pacific (see Supplementary Information). These two sites span the temperature range suitable for the growth of *Diploastrea* and, together, they yield the most 'universal' Sr/Ca–SST calibration available. The slope of the Sr/Ca–SST calibration for *Diploastrea* parallels, within error, the Sr/Ca–SST slope for *Porites* (Fig. 1). The uptake of Sr is greater for the slower growing *Diploastrea* than for *Porites*, consistent with kinetic models of stable isotope ratios in hermatypic corals[19,20]. However, the precision of the reconstructed SST is three times lower for *Diploastrea* than for *Porites* for reasons that are unclear.

The assemblages from the reef bracketing the YD *Diploastrea* in the drill core represent a shallow (<10 m depth) reef environment[17] that is similar to the modern reef settings used for calibration purposes. Decadal variability in skeletal Sr/Ca and δ^{18}O was
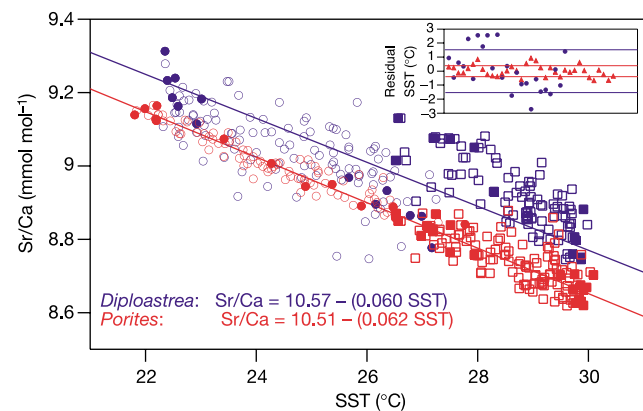

Figure 1 Coral Sr/Ca ratios versus SST. Linear regression between skeletal Sr/Ca and SST for *Diploastrea heliopora* (blue symbols) and *Porites* sp. (red symbols) corals from New Caledonia (circles) and Indonesia (squares). Coral Sr/Ca was regressed against SST using points defining seasonal maxima and minima in the records (represented as filled symbols). Inset, SST residuals represent instrumental SST minus Sr/Ca SST calculated with the regression equations. Lines indicate 1 standard deviation of SST residuals for *Porites* (red) and *Diploastrea* (blue).